6-2001

# Inhibition of the Aminopeptidase from *Aeromonas proteolytica* by l-Leucinephosphonic Acid. Spectroscopic and Crystallographic Characterization of the Transition State of Peptide Hydrolysis

Carin Stamper
*Brandeis University*

Brian Bennett
*Marquette University*, brian.bennett@marquette.edu

Tanya Edwards
*Utah State University*

Richard C. Holz
*Marquette University*, richard.holz@marquette.edu

Dagmar Ringe
*Brandeis University*

*See next page for additional authors*

*Biochemistry*, Vol. 40, No. 24 (1 June 2001): 7035–7046. DOI. 

# Inhibition of the Aminopeptidase from *Aeromonas proteolytica* by l-Leucinephosphonic Acid. Spectroscopic and Crystallographic Characterization of the Transition State of Peptide Hydrolysis

Carin Stamper
Program in Biophysics and Structural Biology, Departments of Biochemistry and Chemistry and Rosenstiel Basic Medical Research Center, Brandeis University, Waltham, Massachusetts
Brian Bennett
Department of Chemistry and Biochemistry, Utah State University, Logan, Utah
Tanya Edwards
Department of Chemistry and Biochemistry, Utah State University, Logan, Utah
Richard C. Holz
Department of Chemistry and Biochemistry, Utah State University, Logan, Utah

Dagmar Ringe
Program in Biophysics and Structural Biology, Departments of Biochemistry and Chemistry and Rosenstiel Basic Medical Research Center, Brandeis University, Waltham, Massachusetts
Gregory Petsko
Program in Biophysics and Structural Biology, Departments of Biochemistry and Chemistry and Rosenstiel Basic Medical Research Center, Brandeis University, Waltham, Massachusetts

SUBJECTS:
X-rays, Peptides and proteins, Metals, Ions, Oxygen

## Abstract

The nature of the interaction of the transition-state analogue inhibitor l-leucinephosphonic acid (LPA) with the leucine aminopeptidase from *Aeromonas proteolytica* (AAP) was investigated. LPA was shown to be a competitive inhibitor at pH 8.0 with a $K_i$ of 6.6 μM. Electronic absorption spectra, recorded at pH 7.5 of [CoCo(AAP)], [CoZn(AAP)], and [ZnCo(AAP)] upon addition of LPA suggest that LPA interacts with both metal ions in the dinuclear active site. EPR studies on the Co(II)-substituted forms of AAP revealed that the environments of the Co(II) ions in both [CoZn(AAP)] and [ZnCo(AAP)] become highly asymmetric and constrained upon the addition of LPA and clearly indicate that LPA interacts with both metal ions. The X-ray crystal structure of AAP complexed with LPA was determined at 2.1 Å resolution. The X-ray crystallographic data indicate that LPA interacts with both metal centers in the dinuclear active site of AAP and a single oxygen atom bridge is absent. Thus, LPA binds to the dinuclear active site of AAP as an η-1,2-μ-phosphonate with one ligand to the second metal ion provided by the N-terminal amine. A structural comparison of the binding of phosphonate-containing transition-state analogues to the mono- and bimetallic peptidases provides insight into the requirement for the second metal ion in bridged bimetallic peptidases. On the basis of the results obtained from the spectroscopic and X-ray crystallographic data presented herein along with previously reported mechanistic data for AAP, a new catalytic mechanism for the hydrolysis reaction catalyzed by AAP is proposed.

Dinuclear metallohydrolases catalyze the degradation of DNA, RNA, phospholipids, and polypetides and are, consequently, key players in carcinogenesis, tissue repair, protein maturation, hormone regulation, cell-cycle control, and protein degradation pathways (*1*−*4*). Examples of enzymes that fall into this class include peptidases, amido- and amidinohydrolases, phosphatases, and nucleases. Therefore, these enzymes are of immense industrial, environmental, and biomedical importance (*5*−*7*). Several dinuclear metallopeptidases retain some catalytic activity as mononuclear enzymes but typically exhibit faster rates with dinuclear active sites. The fact that some peptidases utilize a mononuclear center while others utilize either a mononuclear or dinuclear site but still others require two metal ions to catalyze the same chemical reaction is not well understood. Moreover, with the exception of copper, these enzymes utilize every first row transition metal ion from manganese to zinc. Interestingly, the catalytic role of whatever metal ion is present in these enzymes appears to be the same, i.e., to polarize the carbonyl group for nucleophilic attack, to activate a water molecule to a more nucleophilic hydroxide ion, and/or to stabilize the transition state of the hydrolytic reaction. A comparison of the one- and two-metal peptidases with known X-ray crystal structures reveals some features common to both mono- and dinuclear enzymes (*1*, *8*−*10*). All have at least one metal-bound water molecule, and many have a nonmetal coordinating carboxylate residue, usually a glutamate that forms a hydrogen bond to a metal-bond water molecule.

One of the best-characterized dinuclear metallopeptidases is the aminopeptidase from *Aeromonas proteolytica* (AAP).[1] AAP is a small, thermostable, monomeric enzyme (32 kDa) with a substrate preference for hydrophobic N-terminal amino acid residues (*11*). The native enzyme as isolated requires two Zn(II) ions for full activity; however, the enzyme is approximately 80% active with only one metal ion present. Substitution of the two Zn(II) ions with Co(II), Cu(II), or Ni(II) provides an enzyme that is hyperactive by 7.7-, 6.5-, or 25-fold, respectively, toward certain substrates (*12*−*14*). Bennett and Holz (*15*) recently demonstrated that metal binding to apo-AAP occurs in a sequential fashion, highlighting the potential formation of heterodimetallic sites. Catalytically competent heterodimetallic centers provide systems in which the function of each metal ion can be independently studied by labeling the metal binding sites with spectroscopically active and silent metal ions. The structure of native AAP was determined to 1.8 Å resolution (1AMP) and was shown to contain a single globular domain with a centrally located mixed β-sheet sandwiched between α-helices (*16*). The dinuclear active site contains a (μ-aquo)(μ-carboxylato)dizinc(II) core with a terminal carboxylate and histidine residue at each metal ion, resulting in symmetric coordination spheres for the dinuclear cluster (Figure 1A). Both zinc ions reside in a distorted tetrahedral coordination geometry with a Zn−Zn distance of 3.5 Å. A glutamate residue, Glu151, forms a hydrogen bond with the bridging water molecule, while the second oxygen atom is 3.4 Å from $N^{\varepsilon}$ of His97 which is a ligand to Zn1.

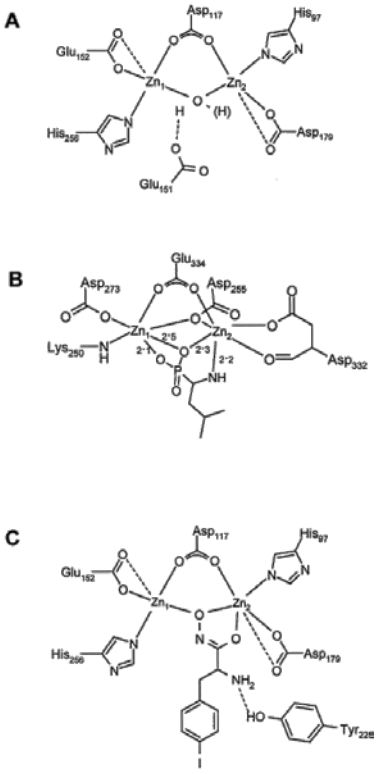


Figure 1 (A) Schematic of the native AAP active site based on the coordinates of PDB entry 1AMP (*16*). The dinuclear center is almost symmetric in that each zinc ion has a ligand donated by a terminal carboxylate and histidine residue, in addition to the bridging aspartate and water molecule. Glu151, also shown, is not a metal ligand but is thought to participate in the hydrolytic reaction. (B) Schematic of LPA bound to the dinuclear center of blLAP, based on the coordinates of entry 1LCP (*22*). Bond distances are shown. The N-terminal amine of LPA interacts with Zn2 of the binuclear cluster. A single oxygen atom acts as a bridge between the two metal ions. A second phosphonate oxygen provides a ligand to Zn1. There is no residue equivalent to Glu151 of AAP in this active site. (C) Schematic of the active site of the AAP−d-IPH complex based on the coordinates of entry 1IGB (*31*). The hydroxylamino oxygen atom bridges the two zinc ions, and the keto group provides a ligand to Zn1. The bridging water/hydroxyl molecule is no longer present. The amino-terminal nitrogen of d-IPH is hydrogen bonded to the phenolic hydroxyl group of Tyr225.

Several inhibitors of AAP have been studied, and these molecules have recently been classified into three types: substrate analogues, tetrahedral transition-state analogues, and simple metal-chelating agents. Examples of the former two types include boronic acids (*17*−*19*), chloromethyl ketones (*11*), and phosphonic acids (*20*−*22*). Among the metal chelators, hydroxamates (*23*−*25*) and α-hydroxyamides (*11*) have been shown to be particularly potent inhibitors of AAP. In the phosphorus-containing transition-state analogue inhibitors, the phosphorus atom is equivalent to the carbon atom that undergoes transformation from $sp^2$ to $sp^3$ hybridization upon nucleophilic attack. For the one-metal peptidases, such as carboxypeptidase A and thermolysin, these compounds are extremely tight binding competitive inhibitors (*9*−*11*). For example, a phophonate tripeptide analogue inhibits carboxypeptidase A with a $K_i$ of 11 fM (*10*, *12*, *13*), while a phophoamidate tripeptide analogue inhibits thermolysin with a $K_i$ of 68 pM (*11*). These same compounds inhibit dinuclear metallopeptidases with significantly less potency. For example, l-leucinephosphonic acid (LPA) is a competitive inhibitor of the leucine aminopeptidase from bovine lens (blLAP) with a $K_i$ of 0.23 μM (*22*). The X-ray crystal structure of blLAP complexed with LPA (*22*) shows that LPA interacts with both metal ions (Figure 1B) and suggests that both metal ions are necessary to stabilize the transition state. In this structure, one phosphonate oxygen atom interacts with Zn1, a second phosphonate oxygen atom bridges the two metal ions, and the N-terminal amine of LPA interacts with Zn2. The two Zn(II) ions are 3.4 Å apart, which is 0.2 Å greater than the separation found in the native structure. An X-ray crystal structure of AAP complexed with d-iodophenylalanine hydroxamate (d-IPH), a simple metal-chelating agent, has also been determined (1IGB) (Figure 1C) (*26*). In this structure, two oxygen atoms of d-IPH serve as ligands to the active site metal ions where the hydroxylamino oxygen atom bridges the two zinc ions. The N-terminal amino group of d-IPH is hydrogen bonded to the phenolic oxygen of Tyr225. However, the stereochemistry of d-IPH is incorrect since AAP only cleaves N-terminal l-amino acid residues, decreasing the mechanistic relevance of the d-IPH−AAP complex.

In an effort to gain insight into the structure of the tetrahedral transition state of peptide hydrolysis, we have explored the inhibition of AAP by l-leucinephosphonic acid (LPA). Analysis of the kinetic data for the interaction of AAP with LPA at pH 8.0, the pH of maximal activity for AAP, shows that LPA is a strong competitive inhibitor. Electronic absorption and EPR spectra of the catalytically competent [CoCo(AAP)], [CoZn(AAP)], and [ZnCo(AAP)] substituted enzymes in the absence and presence of LPA provide insight into the mode of coordination of LPA to AAP (*21*). The exact mode of LPA binding to AAP was elucidated by X-ray crystallographic determination of the structure of the [ZnZn(AAP)]−LPA complex at 2.1 Å. Combination of the X-ray crystallographic and spectroscopic data with the previously reported mechanistic data for AAP has allowed a detailed mechanism of action to be proposed for the metal-mediated peptide hydrolysis reaction catalyzed by AAP.

# Materials and Methods

## Enzyme Purification.

All chemicals used in this study were purchased commercially and were of the highest quality available. LPA was kindly provided by N. Sträter at Harvard University (Cambridge, MA). The aminopeptidase from *A.proteolytica* was purified from a stock culture kindly provided by C. Schalk. Cultures were grown according to the previously published procedure (*11*) with minor modifications to the growth media, the details of which are presented elsewhere (*27*). Crude AAP is associated with two dark brown pigments that partition between the enzyme and octyl-Sepharose column material to different extents. These pigments are only completely removed from the enzyme during the ion exchange chromatography step. Both pigments have intense electronic absorption in the 250−300 nm region. One of the pigments has an electronic absorption maximum at 400 nm and gives rise to an intense isotropic EPR resonance at $g$ = 4.3 indicative of it being associated with Fe(III) (data not shown). The $g$ = 4.3 EPR resonance can therefore be used as a sensitive test for

pigment removal. The purified enzyme used in this study was found not to exhibit the *g* = 4.3 EPR resonance. Denaturing gel electrophoresis indicated that the two resolvable activity-containing fractions from the Q-Sepharose column corresponded to the holoaminopeptidase and a processed form from which 13 N-terminal amino acids have been cleaved ["AP1" and "AP2", respectively in the nomenclature of Schalk et al. (*28*)]. The enzyme was readily crystallized, a stringent test of homogeneity, and was shown to be identical to the structure reported by Chevrier et al. (*16*). The enzyme was stored at 77 K until it was needed.

## Spectrophotometric Assay.

AAP activity was measured by the method of Prescott and Wilkes (*11*) as modified by Baker et al. (*18*). In this assay, the hydrolysis of 0.5 mM l-leucine *p*-nitroanilide (l-*p*NA) [10 mM Tricine (pH 8.0) containing 0.1 mM $ZnSO_4$ or $CoCl_2$] was assessed spectrophotometrically at 25 °C by monitoring the formation of *p*-nitroaniline. The extent of hydrolysis was calculated by monitoring the increase in absorbance at 405 nm ($\Delta\varepsilon_{405}$ value of *p*-nitroaniline = 10 800 $M^{-1}$ $cm^{-1}$). One unit was defined as the amount of enzyme that releases 1 μmol of *p*-nitroaniline at 25 °C in 60 s. Depletion of enzyme-bound zinc or cobalt was prevented by the addition of 0.1 mM $ZnSO_4$ or $CoCl_2$ to the buffer. The specific activity of purified Zn(II)-bound AAP was typically found to be 120 units/mg of enzyme. This value is identical to that reported by Prescott and Wilkes (*11*). Enzyme concentrations were determined from the absorbance at 280 nm with an $\varepsilon_{280}$ of 41 800 $M^{-1}$ $cm^{-1}$ (*29*). The accuracy of this value was checked by the Edelhoch method (*30*−*32*) using a 5:13:2 (molar ratio) *N*-acetyl-l-tryptophanamide/Gly-Tyr-amide/l-cysteine mixture to model AAP. The molar absorptivity determined from this method ($\varepsilon_{280}$ = 43 950 $M^{-1}$ $cm^{-1}$ for AAP solubilized in 6 M guanidine hydrochloride) was in excellent agreement with the value previously reported by Prescott et al. (*29*).

## Kinetic Studies.

The kinetic parameters *v* (velocity), $k_{cat}$ ($V_{max}/[E]_o$), $K_m$ (Michaelis constant), and $K_i$ (inhibition constant) were determined at pH 8.0 by spectrophotometrically recording the initial velocity of the hydrolysis of l-*p*NA at 25 °C in triplicate for both the Zn(II) and Co(II) forms of AAP. LPA concentrations ranged from 0 to 17.5 μM, and velocity values were recorded for each of seven substrate concentrations ranging from 5 to 200 μM. The linearity of the progress curves for product formation both in the absence and in the presence of inhibitor indicates that LAP is in rapid equilibrium with AAP. Depletion of enzyme-bound zinc was prevented by the addition of 0.1 mM $ZnSO_4$ or $CoCl_2$ to all buffers. Because of the addition of excess divalent metal ions to the assay mixture, there is no apoenzyme present. The apoenzyme would likely bind LPA but only very weakly. For example, Ustynyuk et al. (*33*) has previously shown that l-leucine binds to AAP with a $K_i$ of ∼1 mM, but this is nearly 1000 times lower than the $K_i$ value observed for LPA. Buffers used in the pH studies were Tricine (pH 7.5, 8.0, and 8.7) and boric acid (pH 9.0 and 9.5). The inhibitory nature of boric acid was investigated, and it was found to be a weak competitive inhibitor ($K_i$ ∼ 0.3 M). These data are in excellent agreement with the previous results of Baker and Prescott (*17*).

## EPR Samples.

[CoZn(AAP)] and [ZnCo(AAP)] were prepared from the purified enzyme by a method similar to that of Prescott et al. (*13*). Briefly, AAP was dialyzed for 72 h at 4 °C against 10 mM 1,10-phenanthroline monohydrochloride in 50 mM Hepes buffer (pH 7.5) and then exhaustively dialyzed against Chelex-treated Hepes buffer. Metal insertion was effected by direct addition, with efficient mixing, of 1 equiv of $MCl_2$ (where M is Co or Zn; ≥99.999% $CoCl_2$, from Strem Chemicals, Newburyport, MA; 99.999% $ZnCl_2$, from Aldrich) followed by a 30 min incubation period at 20−25 °C. The second metal was then inserted in the same manner and the electronic absorption spectrum recorded prior to freezing in liquid nitrogen for EPR spectroscopy. A 10-fold excess of LPA was introduced onto the inside side wall of an EPR tube and the enzyme sample introduced above this as a plug ∼2 cm in length. As earlier work has demonstrated by optical methods (*34*), violently flicking the above system facilitates rapid and

efficient mixing of the reagents and rapid freezing was achieved by plunging the tube into a beaker of a mixture of liquid and solid methanol over liquid nitrogen.

## Spectroscopic Measurements.

All spectrophotometric measurements were performed on a Shimadzu UV-3101PC spectrophotometer equipped with a constant temperature holder and a Haake (type 423) constant temperature circulating bath. The use of 200 μL, 1 cm path length microcuvettes (QS, Hellma) stoppered with rubber septa facilitated the recording of the optical spectra of EPR samples under anaerobic conditions. Subtraction of the absorption spectrum of apo-AAP from those of the substituted enzymes was performed using Shimadzu UV-3101 software. Low-temperature dual-mode EPR spectroscopy was performed using a Bruker ESP-300E spectrometer equipped with an ER 4116 DM dual-mode X-band cavity and an Oxford Instruments ESR-900 helium flow cryostat as described previously (*15*). Background spectra recorded on an EPR tube containing buffer were aligned with and subtracted from experimental spectra as in earlier work (*34*). Characteristic signals due to oxygen were occasionally observed in both EPR modes. These signals routinely disappeared upon increasing the temperature in the helium cryostat to 125 K for 5 min and recooling. All spectra were recorded at a modulation frequency of 100 kHz and a modulation amplitude of 1.26 mT (12.6 G) and with a sweep rate of 10 mT/s. Parallel- and perpendicular-mode EPR spectra were recorded at microwave frequencies of ∼9.37 and ∼9.65 GHz, respectively: precise microwave frequencies were recorded for individual spectra to facilitate *g* alignment. Other EPR recording parameters are specified in the figure legends for individual samples. Enzyme concentrations for EPR were typically 1−2 mM. All buffers contained 20% 2-propanol to prevent aggregation at high protein concentrations. The purified enzyme stored for up to 2 weeks at 4 °C in Hepes buffer (pH 7.5) containing 20% (by volume) 2-propanol exhibited no measurable decrease in activity, and comparison of EPR spectra with those recorded on more dilute samples in the absence of 2-propanol indicated that 2-propanol had no effect on the electronic structure of the dinuclear metal center.

## Computer Simulations of High-Spin Co(II) S = $^3/_2$ EPR Spectra.

The protocol for simulation of high-spin Co(II) EPR spectra is described in detail elsewhere (*15*). This method of analysis yields two sets of $g_{eff}$ values: those obtained by simulation of the line shape and those allowed by theory for an isotropic $\mathbf{g}_{real}$ tensor. The latter values are given in parentheses after the former. Where an isotropic $g_{real}$ value is assumed, the correspondence between these two sets of values is a quantitative indication of the validity of the simulation. However, as pointed out by Johnson and co-workers (*35*), $g_{real}$ is often anisotropic, lying in the range of 2.1−2.8, and an anisotropic $g_{real}$ value has to be assumed in some cases. In these cases, the $g_{real}$ values that are given are those consistent with the three $g_{eff}$ values and a single value of *E*/*D*. In principle, information about the zero-field splitting parameter, Δ, can be obtained both from EPR saturation behavior and from *g* values of Co(II) species. However, in practice this can prove to be both difficult and misleading, and arguments against this approach have been outlined (*15, 35*). Furthermore, recent work has demonstrated that for sites of nonideal geometry, as commonly found with protein metal binding centers, even reliably determined zero-field splitting parameters are of little use in predicting the coordination of the metal ion (*36*). Thus, no attempt to determine zero-field splitting parameters, other than *E*/*D*, was made.

## Crystallization, Data Collection, and Processing.

AAP was cocrystallized with LPA using the crystallization conditions reported for the native enzyme (*16*), following preincubation with a 4-fold molar excess of LPA. The inhibitor solution was prepared by titrating the dissolved free acid with 1.0 M NaOH to neutrality before addition of the enzyme to avoid decreasing the pH required for crystallization. The purified AAP (10 mg/mL) in 10 mM Tris (pH 8.0), 10 mM KSCN, 0.4 M NaCl, and a 4-fold molar excess of LPA was crystallized by vapor diffusion using 100 mM Tris (pH 8.0), 100 mM KSCN, and 4.5 M NaCl as the precipitating solution. Crystals with dimensions of 0.5 mm × 0.3 mm × 0.3 mm were obtained in 4

days and were shown to be isomorphous with the native crystals. The crystals belong to space group $P6_122$ with the following unit cell dimensions: $a = b = 107.8$ Å, $c = 102.5$ Å, $\alpha = \beta = 90°$, and $\gamma = 120°$. There is one monomer per asymmetric unit.

Diffraction data were collected at 4 °C on an R-axis IIC image plate area detector mounted on a Rigaku RU-200B rotating anode generator operating at 45 kV and 120 mA. A 0.3 mm collimator was used, and the crystal−detector distance was 100 mm. One crystal was used to collect the entire data set. Twenty-five minute exposures were taken with an oscillation step size of 0.5°. The diffraction data were integrated and scaled using the HKL software package (Denzo and Scalepack) (*20*). The data processing and refinement statistics are outlined in Table 1. The data were collected with a high redundancy where 94.2% of the reflections were measured four times or more and 29% of the observed reflections measured nine to twelve times. The overall completeness of the data is 99.9%, including 100% completeness in the outermost shell (2.2−2.1 Å). The $R_{merge}$ in the outer shell was 68.5%, resulting in an overall $R_{merge}$ of 18.1% for the entire data set. Ultimately, the decision to keep all of the data to 2.1 Å was based on the quality of the electron density maps when these data were included.

**Table 1: Data Collection and Refinement Statistics**

| | |
|---|---|
| Crystal Data | |
| space group | $P6_122$ |
| unit cell parameters (Å) | $a = 107.8$, $b = 107.8$, $c = 102.6$ |
| Data Processing | |
| no. of observed reflections | 349668 |
| no. of unique reflections | 21129 |
| cutoff ($I/\sigma$) | 0 |
| $R_{merge}$[a] (outer shell) (%) | 13.4 |
| completeness, overall (%) | 99.9 |
| highest-resolution shell (Å) | 2.17−2.1 |
| completeness, outer shell (%) | 100 |
| Model Refinement | |
| resoloution range (Å) | 10−2.1 |
| cutoff ($F/\sigma F$) | 0 |
| $R$-factor[b] (%) | 19.8 |
| $R_{free}$ (%) | 23.2 |
| no. of protein atoms | 2211 |
| no. of zinc ions | 2 |
| no. of LPA atoms | 10 |
| no. of water molecules | 129 |
| $B$-factor model | individual |
| rmsd from ideality | |
| bond lengths (Å) | 0.006 |
| bond angles (deg) | 1.153 |
| improper angles (deg) | 0.639 |
| dihedral angles (deg) | 25.931 |
| residues in most favored positions[c] (%) | 86.4 |

[a] $R_{merge} = \sum|I_{obs} - I_{avg}|/\sum|I_{avg}|$. [b] $R$-factor $= \sum|F_{obs} - F_{calc}|/\sum|F_{obs}|$. [c] As determined by the program PROCHECK.

## Structure Solution and Refinement.

Since the crystal of the LPA-inhibited AAP was isomorphous with that of the native enzyme, the phases from the published native structure (1AMP) were used as the starting model (*16*). In this process, the zinc atoms and

water molecules were omitted from the original coordinate file. All refinement procedures were carried out using the software package X-PLOR(c) (*21*). An $R_{free}$ (*22*) data set was made using 10% of the unique reflections. The initial model was subjected to two rigid body refinements, the first using reflections in the 12.0−6.0 Å range and the second reflections in the 12.0−4.0 Å range. Subsequent rounds of positional refinement were carried out using higher-resolution data incrementally to 2.1 Å. Difference electron density maps were then calculated ($3F_{obs} - 2F_{calc}$) (*23, 24*) and showed clear electron density in the active site for the bound inhibitor and the missing zinc ions. The *R*-factor and $R_{free}$ at this point were 27 and 31%, respectively. The two zinc ions and several obvious water molecules were added, and the model was subjected to further rounds of positional refinement. The electron density maps calculated for the remainder of the refinement process were calculated with $2F_{obs} - F_{calc}$ and $F_{obs} - F_{calc}$ coefficients. A model for LPA was built using Insight (Molecular Simulations, Inc.), and the model was built into the electron density. Additional water molecules were added to the model using the WATERPICK protocol in the X-PLOR program. The electron density for one water molecule was larger than that for the other water molecules, and the *B*-factor for this atom refined to an unusually low value of 2. In addition, there were five atoms within 2.8 Å of this water molecule: one of the phosphoryl oxygens of the LPA molecule (2.6 Å), two water molecules (2.2 and 2.4 Å), and one oxygen of the terminal carboxylate of Glu151 (2.6 Å). This atom was later modeled as a potassium ion and the *B*-factor then refined to 30 Å. Further rounds of positional as well as both overall and individual *B*-factor refinement resulted in a final structure with an *R*-factor and $R_{free}$ of 19.8 and 23.2%, respectively. In addition to the 291 amino acid residues, the final model contains 2 zinc ions, 129 water molecules, 1 potassium ion, and 10 atoms of the inhibitor molecule (Table 1). Simulated annealing omit maps, in which the active site region was omitted, were calculated and confirmed the presence of the bound inhibitor.

## Results and Discussion

Despite their ubiquity and the wealth of structural information available for dinuclear hydrolytic enzymes, little is known about how these structural motifs relate to function. Of the aminopeptidases, X-ray crystal structures are available for the bovine lens leucine aminopeptidase (blLAP) (*22, 37*), the methionyl aminopeptidases from *Escherichia coli* (*38, 39*), *Pyrococcus furiosus* (*40*), and *Homo sapiens* (*41*) (MetAP's), the aminopeptidase from *Streptomyces griseus* (SAP) (*42*), and the aminopeptidase from *A. proteolytica* (AAP) (*16*). Previous kinetic, spectroscopic, and crystallographic studies on aminopeptidases have focused primarily on the native enzyme structure and that of the substrate-binding step of peptide hydrolysis (*13*, *15*, *16*, *26*, *27*, *33*, *43*, *44*). Either characterization of the transition state of AAP-catalyzed peptide hydrolysis has been limited to kinetic and spectroscopic data, and an X-ray crystal structure of d-IPH bound to AAP (*26*). However, amino acid hydroxamates are simple metal chelators and, therefore, do not represent the transition state of peptide hydrolysis. To gain insight into the structure of the transition state of peptide hydrolysis, the inhibition of AAP by LPA was examined by kinetic, spectroscopic, and X-ray crystallographic methods. A preliminary spectroscopic study on the binding of LPA to AAP has been previously reported (*21*).

### Kinetic Studies.

Initially, the rates of hydrolysis of l-*p*NA were monitored spectrophotometrically as a function of LPA concentration in 10 mM Tricine buffer (pH 8.0) containing 0.1 mM $ZnSO_4$ or $CoCl_2$. Triplicate activity assay determinations at five LPA concentrations (0−17.5 μM) were made for each of seven substrate concentrations (5−200 μM). The linearity of the progress curves for product formation both in the absence and in the presence of inhibitor indicates that LPA is in rapid equilibrium with AAP. The results for [ZnZn(AAP)] are shown in Figure 2 as a double-reciprocal plot of $1/v$ versus 1/[S], which shows a pattern indicative of competitive inhibition. The experimental data were fit to the Michaelis−Menten equation for competitive inhibition reported by Cleland (*45*). The Michaelis constant, $K_m$, for l-*p*NA binding to AAP was found to be 10 μM, and the catalytic constant, $k_{cat}$, was found to be 4320 $min^{-1}$. Both of these values are in excellent agreement with those previously

reported. Plots of 1/*v* and [S]/*v* versus [LPA] (data not shown) yield values for the inhibition constant, $K_i$, for the binding of LPA to AAP of 6.6 ± 0.4 and 5.5 ± 0.4 μM for [ZnZn(AAP)] and [CoCo(AAP)], respectively. The intercept of the plots of 1/*v* versus 1/[S] when 1/[S] = 0 (Figure 2) and the parallel plots of [S]/*v* versus [LPA] (data not shown) clearly demonstrate that LPA is a pure competitive inhibitor of the hydrolysis of l-*p*NA by AAP (*46*). The pH dependence of LPA binding to [ZnZn(AAP)] was also investigated at pH 9.5. The results indicate that the mechanism of inhibition at pH 9.5 is also purely competitive with a $K_i$ similar to that observed at pH 8.0. On the basis of these data and the fact that LPA is a strong competitive inhibitor of blLAP with a $K_i$ of 0.23 μM at pH 8.0 (*22*), LPA likely binds to AAP differently than blLAP.

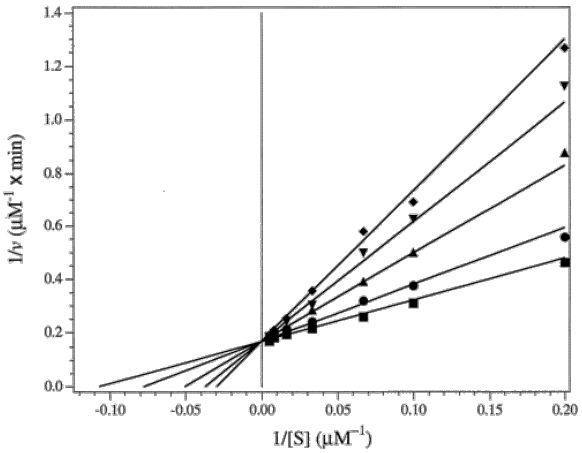


Figure 2 Double-reciprocal plot of 1/*v* vs 1/[S]. The symbols correspond to LPA concentrations of 0, 2.5, 7.5, 12.5, and 17.5 μM. Assays were carried out at 25 °C in 10 mM Tricine buffer (pH 8.0) containing 0.1 mM $ZnSO_4$.

## Spectroscopic Investigations.

To ascertain the nature of any geometrical change that might occur at the dinuclear active site of AAP upon LPA binding, electronic absorption spectra of the catalytically competent [CoCo(AAP)], [CoZn(AAP)], and [ZnCo(AAP)] forms were recorded in the absence and presence of LPA (*21*). The absorption due to apo-AAP was subtracted in each case. The absorption spectrum of [CoCo(AAP)] (Figure 3) reveals an absorption maximum of 525 nm and a molar absorptivity (ε) of ∼85 $M^{-1}$ $cm^{-1}$. The addition of LPA to [CoCo(AAP)] shifts the observed $\lambda_{max}$ from 525 to 500 nm with a concomitant increase in the absorption coefficient from 85 to 130 $M^{-1}$ $cm^{-1}$. Furthermore, the electronic absorption spectrum of the [CoCo(AAP)]−LPA complex exhibits fine structure that is clearly resolved in the first-derivative spectrum, d*A*/dλ versus λ (Figure 3, inset), as comprising five absorption bands at 488, 517, 549, 579, and 601 nm. The increase in the absorption coefficient and the appearance of fine structure are indications that the geometry around one or both of the Co(II) ions is significantly altered upon LPA binding and directly demonstrate interaction of LPA with the dinuclear catalytic metal center. The absorption spectra of [CoZn(AAP)] (58 $M^{-1}$ $cm^{-1}$; Figure 4) and [ZnCo(AAP)] (29 $M^{-1}$ $cm^{-1}$; Figure 4) provide absorption coefficients that are essentially the sum of the absorption coefficient of [CoCo(AAP)] (85 $M^{-1}$ $cm^{-1}$), indicating that the individual Co(II) ions in [CoZn(AAP)] and [ZnCo(AAP)] adopt very similar coordination geometries in their respective substituted enzyme forms as they do in the dinuclear center of [CoCo(AAP)]. Upon the addition of LPA to [CoZn(AAP)], the $\lambda_{max}$ of 525 nm was not perturbed but the molar absorptivity increased from 58 to 68 $M^{-1}$ $cm^{-1}$ (Figure 4). On the other hand, the addition of LPA to [ZnCo(AAP)] markedly affects the electronic absorption spectrum as evidenced by the large increase in the absorption coefficient to 63 $M^{-1}$ $cm^{-1}$ (Figure 4) Interestingly, the observed $\lambda_{max}$ exhibited the same characteristic blue shift as that of [CoCo(AAP)] from 525 to 500 nm. The spectrum also exhibits the fine structure pattern that was also observed for LPA bound to [CoCo(AAP)]. These data indicate that LPA interacts with both metal binding sites in AAP.

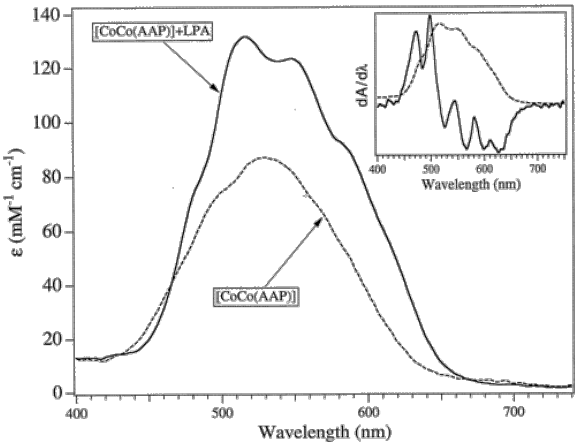

Figure 3 Electronic absorption spectrum of [CoCo(AAP)] in the absence (- - -) and presence (—) of 5 equiv of LPA. The inset shows the electronic absorption spectrum of the [CoCo(AAP)]−LPA complex (- - -) and the first derivative of the absorption, $\delta A/\delta\lambda$ (—).

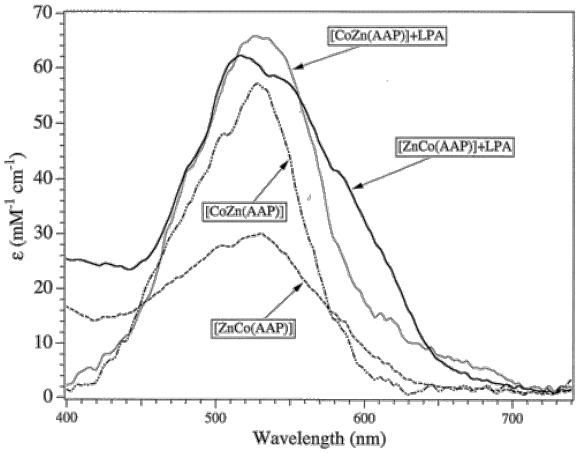

Figure 4 Electronic absorption spectra of [CoZn(AAP)] (–···–), [ZnCo(AAP)] (- - -), the [CoZn(AAP)]−LPA complex (···), and the [ZnCo(AAP)]−LPA complex (—). The latter two samples contain 5 equiv of LPA.

EPR spectra of [CoCo(AAP)] in the absence and presence of LPA were also recorded in both the perpendicular and parallel modes (Figure 5). In the absence of LPA, the perpendicular-mode EPR spectrum reveals an $M_s = |\pm^1/_2\rangle$ ground-state transition with an isotropic $g_{real}$ of 2.25 and an $E/D$ of 0.095, which accounts for only 13% of the expected spin density, suggesting that the two Co(II) ions are spin-coupled, as previously reported (*15*). The addition of LPA to [CoCo(AAP)] completely abolished the perpendicular-mode signal (*21*). These data suggest that the spin coupling between the two Co(II) ions is markedly enhanced upon LPA binding and that LPA must bind to both Co(II) ions. Examination of the [CoCo(AAP)]−LPA complex in the parallel mode revealed an intense signal with a crossover point at $g \sim 10.3$ at 9 K. This signal is likely due to ferromagnetic coupling between two pseudo $S = {}^1/_2$ Co(II) ions with large $g_{real}$ values (>2.5), yielding a pseudo $S = 1$ system. The observation of ferromagnetic coupling between the two high-spin Co(II) ions suggests a spin−spin pathway between the two metal centers. On the basis of the reported magnetic properties of several μ-aquo or (μ-hydroxo)dicobalt(II) model complexes, one would expect weak to moderately strong antiferromagnetic coupling (*47*−*49*). Moreover, bis(μ-carboxylato)- and tetrakis(μ-carboxylato)dicobalt(II) cores also show very weak antiferromagnetic spin coupling (*50*−*52*). These data suggest that a single oxygen atom bridge is not present in the LPA−AAP complex and that the ferromagnetic spin-coupling interaction is not mediated through the carboxylate bridge.

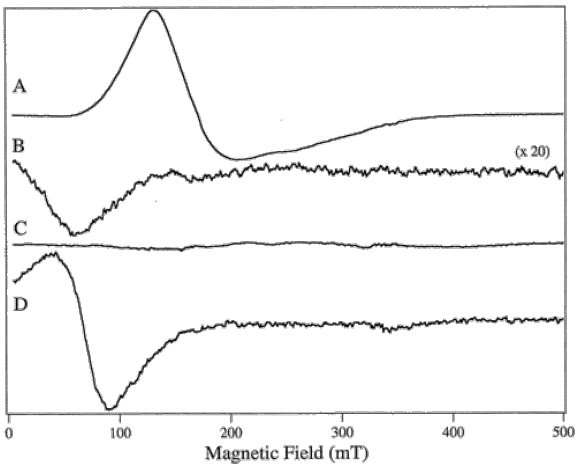


Figure 5 EPR spectra of [CoCo(AAP)]. (A) Perpendicular mode in the absence of LPA. (B) Parallel mode in the absence of LPA. (C) Perpendicular mode in the presence of 5 equiv of LPA. (D) Parallel mode in the presence of 5 equiv of LPA. All samples were buffered with 50 mM Hepes (pH 7.5) containing 20% 2-propanol to prevent aggregation. Perpendicular-mode spectra were recorded at 10 K with a microwave power of 0.2 mW, while parallel-mode spectra were recorded at 3.9 K with a microwave power of 2 mW. All spectra were recorded using a modulation amplitude of 1.26 mT and a sweep rate of 10 mT/s.

The EPR spectrum of [CoZn(AAP)] was also recorded and simulated as previously described (Figure 6A). Upon addition of LPA to [CoZn(AAP)], a dramatic change in the EPR spectrum is observed. A rhombic, $^{59}$Co hyperfine split species is observed that can be simulated as a single species with the parameters $g_{\mathrm{eff}(x,y,z)}$ = 1.90 (2.08), 3.05 (3.04), 6.66 (6.64) (the values given are those used for the line shape simulation, whereas those in parentheses are the closest theoretically allowed values for an isotropic $g_{\mathrm{real}}$ value; see Materials and Methods), corresponding to an $M_s = |\pm^1/_2\rangle$ ground-state transition with an isotropic $g_{\mathrm{real}}$ of 2.53 and an $E/D$ of 0.26. While EPR cannot give direct information regarding coordination geometries or coordination numbers of Co(II) ions, it does provide information regarding electronic structure. From simulation of EPR spectra, both $E/D$ and $g_{\mathrm{real}}$ values are readily obtained. Both of these parameters hold information regarding symmetry; high $g_{\mathrm{real}}$ values reflect extensive spin−orbit coupling, suggestive of low symmetry, and $E/D$ (the rhombic distortion on the axial ligand field) is a direct indication of the deviation from the idealized axial geometry of the ion. Furthermore, anisotropy of $g_{\mathrm{real}}$ can be taken as an indicator of the asymmetric distribution of the paramagnetic electron density about the metal ion, reflecting any asymmetry in the electric field gradient across the ion due to the ligand sphere.

For the [CoZn(AAP)]−LPA complex, agreement between the two highest $g_{\mathrm{eff}}$ values obtained from the line shape simulation and by theory is excellent; however, agreement between the experimentally derived and theoretically derived lowest $g_{\mathrm{eff}}$ value is poor. The three $g_{\mathrm{eff}}$ values, which are in good agreement with those obtained by line shape simulation, correspond to a unique value for $E/D$ but cannot be derived from theory for a system with an isotropic $g_{\mathrm{real}}$ value. These data suggest that $g_{\mathrm{real}}$ is in fact anisotropic, and exact agreement between experiment and theory for an $E/D$ of 0.26 is obtained by assuming an axial $g_{\mathrm{real}}$ with a $g_x$ of 2.31 and a $g_{y,z}$ of 2.54. It should be noted that while these parameters represent a unique solution assuming $g_y = g_z$, many solutions exist if one allows $g_x$, $g_y$, and $g_z$ to all differ. Nevertheless, the range of solutions that yield three reasonable $g_{\mathrm{real}}$ values is actually quite small. For example, assuming an $E/D$ value of 0.2 yields $g_x$, $g_y$, and $g_z$ values of 2.93, 2.82, and 2.36, respectively, of which $g_x$ and $g_y$ are unreasonably large. Similarly, assuming an $E/D$ value of 0.33 yields $g_x$, $g_y$, and $g_z$ values of 2.42, 2.06, and 2.55, respectively, of which $g_y$ is below the usual lower limit (2.1) for Co(II) ions. Therefore, a reasonable estimate of the error in $E/D$ for an anisotropic system is ±0.04. The $E/+D$ value for the [CoZn(AAP)]−LPA complex of 0.26, therefore, can only correspond to a

highly rhombically distorted axial zero-field splitting. Further support for this conclusion comes from the clearly resolved $^{59}$Co hyperfine splitting and the similarity of the signal to the hyperfine split $g$ = 2.54 signal observed in [CoZn(AAP)] (Figure 6C). Simulation of the latter (Figure 6D) assumes an $E/D$ of 0.32, and unlike the [CoZn(AAP)]−LPA complex, a solution can be obtained assuming an isotropic $g_{real}$ value which is, therefore, unique; consequently, the error in the estimation of $E/D$ is very small (less than ±0.01). Thus, the $g$ = 2.54 signal of resting [CoZn(AAP)] certainly corresponds to a highly distorted electronic environment of the Co(II) ion. The similarity of the EPR spectrum of the [CoZn(AAP)]−LPA complex is strong circumstantial evidence that it, too, is of low symmetry. Further, the presence of resolved $^{59}$Co hyperfine splitting with both a similar line width and $A_z(^{59}Co)$ strongly suggests that the two species are correspondingly free of $g$ strain and thus both are geometrically highly constrained by the ligand field. Finally, the fact that the [CoZn(AAP)]−LPA complex is a single species implies that unlike all the other mono-Co(II) signals observed for AAP thus far, the geometry must be sufficiently constrained so as to preclude the appearance of the structural microheterogeneities which give rise to the $g$ strain, $A$ strain, and $E/D$ strain responsible for the presence of multiple species. Thus, it appears that LPA binding locks the Co(II) ion in [CoZn(AAP)] into a very definite, defined coordination geometry, which must be the result of direct ligation of the Co(II) ion by LPA.

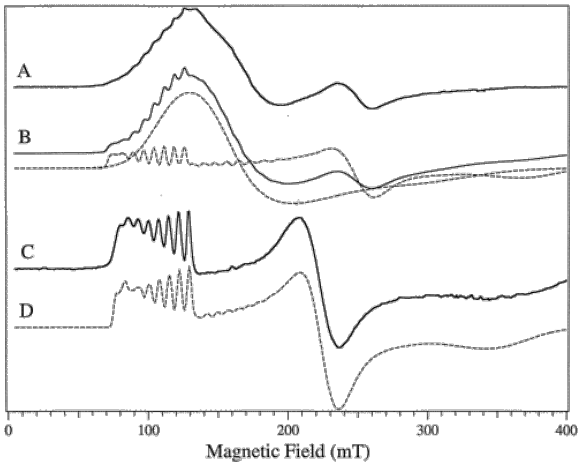


Figure 6 EPR spectra of [CoZn(AAP)]. (A) In 50 mM Hepes buffer (pH 7.5) containing 20% 2-propanol. (B) Simulation of spectrum A (—) assuming two species (- - -) with $g_{eff(x,y,z)}$ = 2.20, 3.92, 5.23; $M_s$ = $|\pm^1/_2\rangle$ ; $g_{real}$ = 2.29; and $E/D$ = 0.10 and $g_{real(xyz)}$ = 1.80, 2.75, 6.88; $A_z(^{59}Co)$ = 7.0 mT; $M_s$ = $|\pm^1/_2\rangle$ ; $g_{real}$ = 2.54; and $E/D$ = 0.32. (C) In 50 mM Hepes buffer (pH 7.5) after the addition of 5 equiv of LPA. (D) Simulation of spectrum C assuming $g_{eff(x,y,z)}$ = 1.90, 3.05, 6.66; $A_z(^{59}Co)$ = 7.0 mT; $M_s$ = $|\pm^1/_2\rangle$ ; $g_{real(x,y,z)}$ = 2.31, 2.54, 2.54; and $E/D$ = 0.26. All spectra were recorded at 10 K and 0.2 mW, with a modulation amplitude of 1.26 mT and a sweep rate of 10 mT/s.

The EPR spectrum of [ZnCo(AAP)] is shown in Figure 7 and has been described in earlier work (*15*). Upon addition of LPA to [ZnCo(AAP)], a dramatic change in the EPR spectrum is observed (*21*). The spectrum and a computer simulation are presented in panels B and C of Figure 7, respectively. The simulation invoked a single species with $g_{eff}$ values of 6.23, 3.40, and 1.95 and an $A_z(^{59}Co)$ of 4.95 mT. These values correspond to an axial $g_{real}$ value where $g_{x,y}$ = 2.204, which gives rise to the resonance at $g_{eff}$ = 1.95 and $g_z$ = 2.48. The rhombic distortion of the axial field $E/D$ = 0.20. This value is somewhat lower than that for the Co(II) ion in [CoZn(AAP)]. Interestingly, the $^{59}$Co hyperfine splitting is significantly smaller than that observed for other Co(II)-substituted AAP species, and suggests delocalization of some 30% of the paramagnetic electron density from the cobalt nucleus. This implies a direct interaction of the Co(II) ion with an electrophilic moiety such as the N-terminal amine group of LPA as was observed for LPA binding to blLAP by X-ray crystallography (*22*). Delocalization of electron density onto a ligand atom orbital is also consistent with the anisotropy of $g_{real}$ for this

species. These data suggest that electron density donation by the second metal may be important in stabilizing the transition state and thus suggests a role for the second metal ion in catalysis.

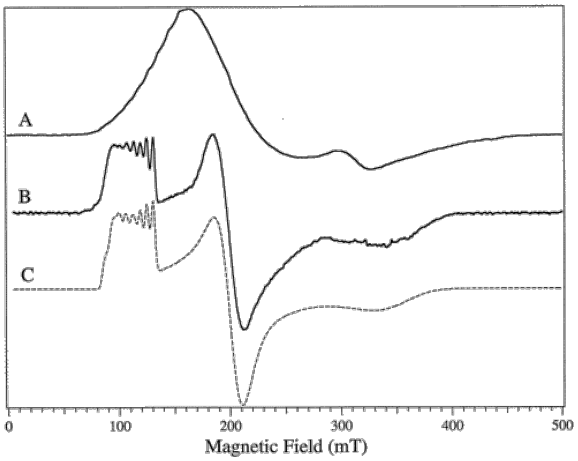


Figure 7 EPR spectrum of [ZnCo(AAP)] (A) in 50 mM Hepes buffer (pH 7.5) containing 20% 2-propanol and (B) in the presence of 5 equiv of LPA. (C) Simulation of spectrum B assuming $g_{\mathrm{eff}(x,y,z)}$ = 6.23, 3.40, 1.95; $A_z(^{59}\mathrm{Co})$ = 4.95 mT; $M_s = |\pm^1/_2\rangle$ ; $g_{\mathrm{real}(x,y,z)}$ = 2.20, 2.20, 2.48; and $E/D$ = 0.20. The experimental spectrum was recorded at 10 K and 0.2 mW, with a modulation amplitude of 1.26 mT and a sweep rate of 10 mT/s.

## X-ray Crystal Structure of the [ZnZn(AAP)]−LPA Complex.

While spectroscopic studies suggest that LPA binds to both metal ions of the dinuclear active site of AAP, the only way to definitively determine the exact binding nature of LPA is by X-ray crystallography. Therefore, we have crystallized AAP in the presence of LPA and have determined the X-ray crystal structure to 2.1 Å resolution (Figure 8). Inhibitor binding does not introduce major conformation changes into the protein, and the structures of the native AAP and AAP−LPA complex agree very well with an rms deviation of 0.21 Å for the 291 structurally equivalent Cα atoms. The two Zn(II) atoms are 3.9 Å apart in the LPA complex (Figure 9) compared to 3.5 Å in the native structure. This difference is significant at this resolution since the error in the coordinates is approximately 0.3 Å. The leucine group of LPA resides in a well-defined hydrophobic pocket adjacent to the dinuclear Zn(II) active sites. For AAP, this site is made up of Met180, Ile193, Cys223, Tyr225, Cys227, Met242, Phe248, Tyr251, and Ile255. The two Cys residues form a disulfide bond at the back of this pocket, and on the basis of previous X-ray crystallographic data as well as a recent kinetic study, this pocket was shown to be the initial substrate recognition point on the enzyme (*16, 26*).

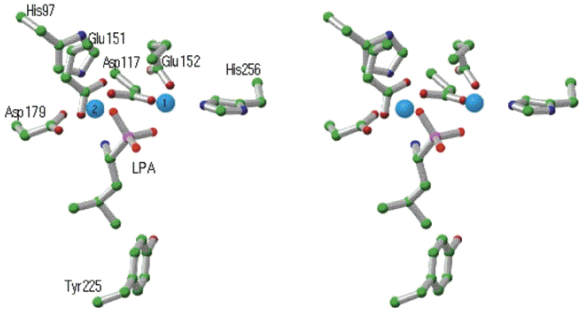


Figure 8 Stereoimage of the AAP−LPA complex active site. LPA binds to the binuclear center with one of the ligands at Zn2 provided by the N-terminal amine and another by O3 of LPA. The LPA O1 atom provides a ligand to Zn1. The bridging water/hydroxide molecule found in the native structure is not present in the AAP−LPA complex.

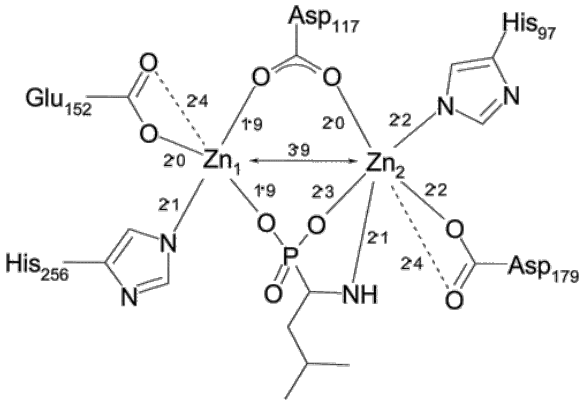


Figure 9 Schematic of the active site in the AAP−LPA complex with distances (in angstroms) shown for all ligands to the zinc ions. Some of the residues involved in van der Waals interactions with the side chain of the inhibitor have been omitted for clarity.

The amino acid residues ligated to the dizinc(II) cluster are identical to those in the native structure with only minor perturbations in the bond lengths (Table 2 and Figure 9). Zn1 of the [ZnZn(AAP)]−LPA complex resides in a distorted tetrahedral environment, while Zn2 exhibits a distorted five-coordinate geometry. Glu152 is coordinated in an asymmetric bidentate fashion to Zn1 with the additional oxygen atom providing a potential fifth ligand at a distance of 2.4 Å. Similarly, Asp179 is coordinated to Zn2 in an asymmetric bidentate fashion with the second oxygen atom residing 2.4 Å from the metal center, providing a potential sixth ligand. Two of the LPA oxygen atoms are coordinated to the two Zn(II) ions in the active site. Namely, O1 is 1.9 Å from Zn1 and 3.4 Å from Zn2, while O3 is 3.3 Å from Zn1 and 2.3 Å from Zn2. There are no binding interactions between any single atom of LPA and both zinc ions; the phosphonate oxygen atom, O3, is coordinated to Zn2, and O1 is coordinated to Zn1. Moreover, there is no electron density between the two Zn(II) ions, suggesting that a bridging water molecule does not exist. A hydrogen bond (3.0 Å) also exists between Glu151 and the O3 atom of the phosphonate moiety. Since Glu151 forms a hydrogen bond with the bridging water/hydroxide molecule in the native structure, the O3 atom of the phosphonate group likely represents the nucleophilic oxygen atom. Finally, the $NH_2$ group of LPA, which mimics the N-terminal amine group of an incoming peptide, is 2.1 Å from Zn2. The X-ray crystallographic data indicate that LPA interacts with both metal centers and a single oxygen atom bridge is absent. Thus, LPA binds to the dinuclear active site of AAP as an η-1,2-μ-phosphonate with one ligand to the second metal ion provided by the N-terminal amine (Figure 9).

**Table 2: Selected Bond Lengths (Å) for the Zinc−Ligand Distances in the AAP−LPA Complex**

| | zinc−ligand distance (Å) | | |
|---|---|---|---|
| zinc−ligand | native | BuBA complex | LPA complex |
| Zn1−Zn2 | 3.5 | 3.3 | 3.9 |
| Zn1−Asp117 O2 | 2.1 | 2.2 | 1.9 |
| Zn1−Glu152 O1 | 2.0 | 2.2 | 2.0 |
| Zn1−Glu152 O2 | 2.4 | 2.6 | 2.4 |
| Zn1−His256 N2 | 2.3 | 2.3 | 2.1 |
| Zn1−$H_2O$ | 2.3 | − | − |
| Zn1−BuBA O1 | − | 2.5 | − |
| Zn1−BuBA O2 | − | 2.7 | − |
| Zn1−LPA O1 | − | − | 1.9 |
| Zn2−Asp117 O1 | 2.0 | 2.1 | 2.0 |
| Zn2−Asp179 O1 | 2.1 | 2.2 | 2.2 |
| Zn2−Asp179 O2 | 2.3 | 2.5 | 2.4 |

| | | | |
|---|---|---|---|
| Zn2−His97 N2 | 2.3 | 2.2 | 2.2 |
| Zn2−$H_2O$ | 2.3 | – | – |
| Zn2−BuBA O2 | – | 3.0 | – |
| Zn2−BuBA O1 | – | 4.4 | – |
| Zn2−LPA O3 | – | – | 2.3 |
| Zn2−LPA $NH_2$ | – | – | 2.1 |

According to the X-ray structure of the [ZnZn(blLAP)]−LPA complex (*22*), the transition-state analogue binds to both metal ions through the $PO_3$ moiety with a single oxygen atom of LPA bridging the dinuclear center (i.e., an η-1-μ-phosphonate). This is distinctly different from the mode of binding of LPA to AAP, which does not have a single oxygen atom bridge. However, both structures imply that the transition state of peptide hydrolysis is stabilized by coordination of the gem-diol oxygen atoms to both metal ions and the N-terminal amine to one metal ion [i.e., the peptide carbonyl group binds to one or both Zn(II) ions and the N-terminal amine binds to the second Zn(II) ion]. Therefore, both metal ions are required for full enzymatic activity in both lbLAP and AAP, but their individual roles in catalysis appear to differ even though both enzymes have nearly identical substrate specificities.

## Mechanistic Implications.

Combination of all of the reported kinetic, thermodynamic, spectroscopic, and X-ray crystallographic data reported to date with the data presented herein has allowed a detailed mechanism of action to be proposed for the peptide hydrolysis reaction catalyzed by AAP (Figure 10). On the basis of kinetic measurements of the level of aliphatic alcohol binding to AAP, the incoming N-terminal peptide leucine group interacts with Phe244, Phe248, Tyr251, and Tyr255 in the hydrophobic pocket adjacent to the dinuclear active site (*33*). This binding scheme is consistent with the large negative entropy and large positive enthalpy of activation reported for AAP (*27*). An active site carboxylate group, Glu151, was implicated in the catalytic process from X-ray crystallographic data since Glu151 forms a hydrogen bond with the bridging water/hydroxide molecule in the resting enzyme (*16*). We propose that the carbonyl oxygen atom of the incoming peptide binds to Zn1. This is consistent with both EPR spectroscopic studies and the X-ray crystal structure of AAP in the presence of the substrate analogue inhibitor BuBA which binds only to the first metal binding site (*15*, *43*, *44*). Bennett and Holz (*15*) recently demonstrated that metal binding to apo-AAP occurs in a sequential fashion. It was also shown, on the basis of electronic absorption and EPR spectroscopy, that the spectroscopic signatures for [Co_(AAP)] and [CoZn(AAP)] were identical but distinct from those of [ZnCo(AAP)]. Combination of these data with the X-ray crystallographic results of BuBA binding to AAP (*44*) indicates that the first metal binding site in AAP is the Zn1 site.

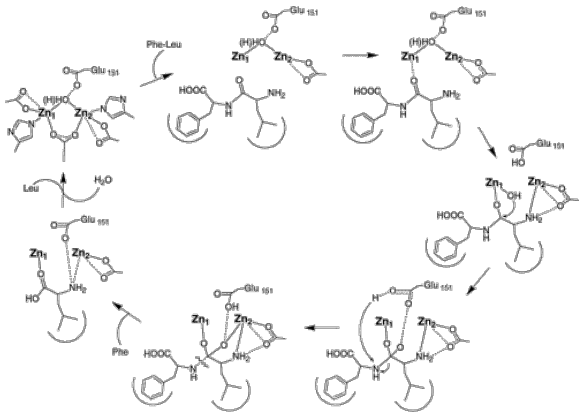


Figure 10 Proposed mechanism of peptide hydrolysis catalyzed by AAP. Protein ligands to the metal ions are shown only in the first panel to avoid confusion. The orientation of this scheme is somewhat different from that presented in Figure 9, because in the proposed mechanism, the substrate and the bridging water (hydroxide) are

bound simultaneously. If the mechanism were presented with the bound species in the same orientation as that given in Figure 9, these groups would project on top of one another.

The fact that AAP exhibits 80% of its maximum activity with only a single Zn(II) ion bound and fluoride binding occurs after substrate binding (*27*) suggests that the bridging water/hydroxide molecule becomes terminal upon substrate binding and is bound to the Zn1 binding site. The breaking of the Zn2−OH(H) bond is likely assisted by N-terminal amine binding which is corroborated by the observation that the N-terminal amine group ($RNH_2$) of LPA is coordinated to Zn2. Interestingly, the S atom of Met180, a residue in the hydrophobic pocket adjacent to the dinuclear active site of AAP, is only 3.1 Å from the N-terminal amine group, suggesting a hydrogen bonding interaction. Likewise, the O2 atom of Asp179 is 3.1 Å from the N atom of the N-terminal amine group, also indicating a hydrogen bonding interaction. A similar interaction for the N-terminal amine of LPA has been shown by X-ray crystallography for LPA bound to blLAP (*22*). Moreover, amine binding to the second Mn(II) ion in arginase has been proposed to drive the loss of the bridging water/hydroxide molecule to form a terminal hydroxide that functions as the nucleophile in the hydrolytic reaction (*53*). The breaking of the Zn2−OH(H) bond is likely assisted by N-terminal amine binding as well as Asp99 hydrogen bonding to the Zn2 ligand, His97. The role of Glu151 is likely to assist in the deprotonation of the terminal water molecule to the nucleophilic hydroxo moiety, similar to that of Glu270 in carboxypeptidase A (*37*).

Recently, it was suggested that a combination of several hydrogen bonding interactions may act to destroy the local symmetry of the dinuclear active site cluster as well as decrease the Lewis acidity of the Zn2 ion, thus providing another driving force for breaking the Zn2−OH(H) bond (*44*). Breaking the Zn2−OH(H) bond would leave the putative nucleophile ($OH^-$) and the substrate on the same zinc (Zn1) ion. In this proposal, both the substrate scissile carbonyl carbon and the nucleophile reside on the Zn1 site, thereby positioning a hydroxide for nucleophilic attack. This proposal is consistent with the resent spectroscopic data and the X-ray crystal structure of the substrate analogue inhibitor butaneboronic acid (BuBA) bound to AAP (*15*, *43*, *44*). The [ZnZn(AAP)]−LPA X-ray crystal structure is also consistent with this suggestion in that one of these hydrogen bonding interactions is between an oxygen atom of Glu151 and the coordinated $N^{\varepsilon}$ atom of His97, which is a ligand to Zn2. This distance (3.2 Å) is somewhat shorter than the distance of 3.4 Å found in the native structure and allows for a hydrogen bond between Glu151 and His97 that may not have existed in the native structure, or only existed weakly or transiently. These data suggest that Glu151 may contribute to the regulation of the Lewis acidity of Zn2. A second hydrogen bonding interaction is observed between Asp99 and His97, forming an Asp-His-Zn triad. An oxygen atom of Asp99 is 2.9 Å from the $N^{\delta}$ atom of His97, suggesting a strong hydrogen bonding interaction. This compares to a distance of 2.7 Å in the [ZnZn(AAP)]−BuBA structure and a distance of 2.8 Å in the resting enzyme. Strong hydrogen bonds between active site Asp residues and histidine ligands in zinc metalloproteins have been shown previously to provide a histidinate-like ligand (*54*), thus decreasing the Lewis acidity of Zn(II) ions. For Zn2, coordination of Asp179 and Asp117 results in significant negative charge around the metal ion. Therefore, the hydrogen bond between His97 and Asp99 provides some degree of a histidinate-like ligand, which helps Zn2 modulate its Lewis acidity during catalysis and retain its charge neutrality. If this hydrogen bond is sufficiently strong (the shortest distance occurs for the substrate-bound [ZnZn(AAP)]−BuBA structure), this interaction can decrease the Lewis acidity of Zn2 sufficiently to assist in the loss of the bridging water/hydroxide molecule.

Since AAP can function with only one metal ion present, the second metal ion must be replaced by another active site group or groups when it is absent. For example, the MetAP from *E. coli* is fully active with only a single Co(II) or Fe(II) ion present even though the available X-ray crystallographic data suggest a dinuclear active site (*55*). The divalent metal binding nature of MetAP and AAP also appears to be analogous to those of the zinc-dependent β-lactamase from *Bacillus cereus*. Of the two Zn(II) ions in the active site of the β-lactamase from *B.*

*cereus*, the tightly bound Zn(II) ion is proposed to provide the nucleophile and also act as a Lewis acid to stabilize the tetrahedral transition state (*56, 57*). The role of the second Zn(II) ion is unclear since a conserved carboxylate residue is proposed to act as a general base to form the dianion and also to protonate the leaving group, thus facilitating C−N bond cleavage. It has, therefore, been suggested that the *B. cereus* enzyme may be an evolutionary intermediate between the mono- and dizinc(II) metallo-β-lactamases (*58*). Similarly, X-ray crystallographic data for the MetAP from *E. coli* with a substrate analogue inhibitor bound (*39*) revealed that the N-terminal amine nitrogen is coordinated to the noncatalytic Co(II) ion, which resides in the carboxylate only side of the active site. For a single-metal ion mechanism to exist, it was recently proposed that the catalytic role ascribed to the non-histidine-coordinated metal ion must be performed instead by the active site amino acid group Asp97 and possibly Asp108 and Glu235. These carboxylate residues form a negatively charged pocket in the appropriate position to bind the N-terminal amine moiety. A similar role for Asp179 and possibly Asp117 can be envisioned for AAP when only one Zn(II) ion is bound. Thus, the second metal binding site in AAP plays a catalytic role similar to that of the second metal ion in MetAP by interacting with the N-terminal amine; however, in the absence of a divalent metal ion, the negatively charged carboxylate pocket interacts with the N-terminus, while in the presence of Zn(II), the divalent metal ion binds the N-terminal amine.

The position of the N-terminal amine group in LPA is distinctly different from that observed for the [ZnZn(AAP)]−d-IPH complex (*26*). In the d-IPH complex, the N-terminal amine group is not present in the active site pocket but instead forms a hydrogen bond with Tyr225 near the surface of the enzyme at the mouth of the active site pocket. Conversely, the N-terminal amine in the LPA complex is coordinated to Zn2. Therefore, the conformation of the inhibitor observed in the AAP−d-IPH complex is an inaccurate representation of the actual transition state of peptide hydrolysis; i.e., the stereochemistry of the d-IPH inhibitor is incorrect for an actual peptide since IPH resides in the d-configuration. With this in mind, little mechanistic information can be gleaned from the [ZnZn(AAP)]−d-IPH structure since d-IPH is simply acting as a metal chelator, rather than mimicking either substrate binding or the transition state of the catalytic reaction. Consequently, any mechanistic conclusions derived from the AAP−d-IPH structure likely led to an incorrect assignment for the role of the second metal ion in the peptide hydrolysis reaction catalyzed by AAP (*15, 27*).

LPA provides an excellent mimic for the transition state in the putative reaction pathway of peptide hydrolysis particularly because it has the correct l-configuration for peptide hydrolysis. Therefore, upon nucleophilic attack at the carbonyl $sp^2$ carbon atom of a peptide bond by an active site hydroxyl, the resultant $sp^3$ carbon-containing transition state would be similar in structure to the R-$PO_3$ group of LPA. The fact that no bridging water molecule is present in the AAP−LPA structure and that Glu151 forms a hydrogen bond with the O3 atom of LPA (3.0 Å) is consistent with O3 being the hydroxyl oxygen atom of the nucleophile. The role of Glu151 is likely to assist in the deprotonation of the terminal water molecule to the nucleophilic hydroxo moiety, a role similar to that proposed for Glu270 in carboxypeptidase A (*59*). The coordination of O3 to Zn2 suggests that after nucleophilic attack by the hydroxide ion, the resulting transition state is stabilized by the additional binding interactions via the second metal ion in the dinuclear active site of AAP. At this point in the mechanism, the metal-bound hydroxide can attack the activated scissile carbonyl carbon of the peptide substrate, forming a gem-diolate transition-state intermediate complex that is stabilized by coordination of both oxygen atoms to the dizinc(II) center, consistent with the [ZnZn(AAP)]−LPA structure. Glu151 likely provides an additional proton to the nucleophilic oxygen atom, returning it to its ionized state. Product formation would then be predicted to be the rate-limiting step, which is consistent with recent thermodynamic results (*27*). Finally, the dizinc(II) cluster releases the cleaved peptides and adds a water molecule that bridges the two metal ions. These data suggest that the second metal ion in the dinuclear active site acts to stabilize the transition state of hydrolysis, since a significantly greater number of binding interactions occur in the transition state than in the substrate binding step. Thus, both metal ions are required for the full enzymatic activity of AAP, but their individual roles appear to differ markedly.

## Acknowledgment

We are grateful to Drs. Norbert Sträter and William Lipscomb of Harvard University for kindly providing the inhibitor l-leucinephosphonic acid.

## References

**1** Sträter, N., Lipscomb, W. N., Klabunde, T., and Krebs, B. (1996) *Angew. Chem., Int. Ed. 35*, 2024−2055.
**2** Lipscomb, W. N., and Sträter, N. (1996) *Chem. Rev.96*, 2375−2433.
**3** Wilcox, D. E. (1996) *Chem. Rev.96*, 2435−2458.
**4** Dismukes, G. C. (1996) *Chem. Rev.96*, 2909−2926.
**5** Chin, J. (1991) *Acc. Chem. Res.24*, 145−152.
**6** Lai, K., Dave, K. I., and Wild, J. R. (1994) *J. Biol. Chem.269*, 16579−16584.
**7** Menger, F. M., Gan, L. H., Johnson, E., and Durst, D. H. (1987) *J. Am. Chem. Soc.109*, 2800−2803.
**8** Vallee, B. L., and Auld, D. S. (1990) *Biochemistry29*, 5647−5659.
**9** Vallee, B. L., and Auld, D. S. (1993) *Proc. Natl. Acad. Sci. U.S.A.90*, 2715−2718.
**10** Vallee, B. L., and Auld, D. S. (1993) *Biochemistry 32*, 6493−6500.
**11** Prescott, J. M., and Wilkes, S. H. (1976) *Methods Enzymol.45B*, 530−543.
**12** Prescott, J. M., Wagner, F. W., Holmquist, B., and Vallee, B. L. (1983) *Biochem. Biophys. Res. Commun.114*, 646−652.
**13** Prescott, J. M., Wagner, F. W., Holmquist, B., and Vallee, B. L. (1985) *Biochemistry24*, 5350−5356.
**14** Bayliss, M. E., and Prescott, J. M. (1986) *Biochemistry25*, 8113−8117.
**15** Bennett, B., and Holz, R. C. (1997) *J. Am. Chem. Soc.119*, 1923−1933.
**16** Chevrier, B., Schalk, C., D'Orchymont, H., Rondeau, J.-M., Moras, D., and Tarnus, C. (1994) *Structure2*, 283−291.
**17** Baker, J. O., and Prescott, J. M. (1983) *Biochemistry22*, 5322−5331.
**18** Baker, J. O., Wilkes, S. H., Bayliss, M. E., and Prescott, J. M. (1983) *Biochemistry22*, 2098−2103.
**19** Baker, J. O., and Prescott, J. M. (1985) *Biochem. Biophys. Res. Commun.130*, 1154−1160.
**20** Lejczak, B., Kafarski, P., and Zygmunt, J. (1989) *Biochemistry28*, 3549−3555.
**21** Bennett, B., and Holz, R. C. (1998) *J. Am. Chem. Soc.120*, 12139−12140.
**22** Sträter, N., and Lipscomb, W. N. (1995) *Biochemistry34*, 9200−9210.
**23** Wilkes, S. H., and Prescott, J. M. (1983) *J. Biol. Chem.258*, 13517−13521.
**24** Wilkes, S. H., and Prescott, J. M. (1987) *J. Biol. Chem.262*, 8621−8625.
**25** Chan, W. W.-C., Dennis, P., Demmer, W., and Brand, K. (1982) *J. Biol. Chem.257*, 7955−7957.
**26** Chevrier, B., D'Orchymont, H., Schalk, C., Tarnus, C., and Moras, D. (1996) *Eur. J. Biochem.237*, 393−398.
**27** Chen, G., Edwards, T., D'souza, V. M., and Holz, R. C. (1997) *Biochemistry36*, 4278−4286.
**28** Schalk, C., Remy, J.-M., Chevrier, B., Moras, D., and Tarnus, C. (1992) *Arch. Biochem. Biophys.294*, 91−97.
**29** Prescott, J. M., Wilkes, S. H., Wagner, F. W., and Wilson, K. J. (1971) *J. Biol. Chem.246*, 1756−1764.
**30** Edelhoch, H. (1967) *Biochemistry6*, 1948−1954.
**31** Gill, S. C., and von Hippel, P. H. (1989) *Anal. Biochem.182*, 319−326.
**32** Gill, S. C., and von Hippel, P. H. (1990) *Anal. Biochem.189*, 283.
**33** Ustynyuk, L., Bennett, B., Edwards, T., and Holz, R. C. (1999) *Biochemistry38*, 11433−11439.
**34** Bennett, B., Berks, B. C., Ferguson, S. J., Thomson, A. J., and Richardson, D. J. (1994) *Eur. J. Biochem.226*, 789−798.
**35** Werth, M. T., Tang, S.-F., Formicka, G., Zeppezauer, M., and Johnson, M. K. (1995) *Inorg. Chem.34*, 218−228.
**36** Larrabee, J. A., Alessi, C. M., Asiedu, E. T., Cook, J. O., Hoerning, K. R., Klingler, L. J., Okin, G. S., Santee, S. G., and Volkert, T. L. (1997) *J. Am. Chem. Soc.119*, 4182−4196.
**37** Kim, H., and Lipscomb, W. N. (1993) *Biochemistry32*, 8465−8478.
**38** Roderick, S. L., and Matthews, B. W. (1993) *Biochemistry32*, 3907−3912.
**39** Lowther, W. T., Orville, A. M., Madden, D. T., Lim, S., Rich, D. H., and Matthews, B. W. (1999) *Biochemistry38*, 7678−7688.

**40** Tahirov, T. H., Oki, H., Tsukihara, T., Ogasahara, K., Yutani, K., Ogata, K., Izu, Y., Tsunasawa, S., and Kato, I. (1998) *J. Mol. Biol.284*, 101−124.
**41** Liu, S., Widom, J., Kemp, C. W., Crews, C. M., and Clardy, J. (1998) *Science282*, 1324−1327.
**42** Greenblatt, H. M., Almog, O., Maras, B., Spungin-Bialik, A., Barra, D., Blumberg, S., and Shoham, G. (1997) *J. Mol. Biol.265*, 620−636.
**43** Bennett, B., and Holz, R. C. (1997) *Biochemistry36*, 9837−9846.
**44** DePaola, C., Bennett, B., Holz, R. C., Ringe, D., and Petsko, G. (1999) *Biochemistry38*, 9048−9053.
**45** Cleland, W. W. (1979) *Methods Enzymol.63*, 103−138.
**46** Segel, I. H. (1975) *Enzyme Kinetics: Behavior and analysis of rapid equilibrium and steady-state enzyme systems*, 1st ed., John Wiley & Sons, New York.
**47** Turpeinen, U., Ahlgren, M., and Hämäläinen, R. (1982) *Acta Crystallogr.B32*, 1580−1583.
**48** Turpeinen, U., Hämäläinen, R., and Reedijk, J. (1987) *Polyhedron6*, 1603−1610.
**49** Chaudhuri, P., Ouerbach, J., Wieghardt, K., Nuber, B., and Weiss, J. (1990) *J. Chem. Soc., Dalton Trans.*, 271−278.
**50** Glerup, J., Goodson, P. A., Hodgson, D. J., and Michelsen, K. (1995) *Inorg. Chem.34*, 6255−6264.
**51** Kalinnikov, V. T., Rakitin, Y. V., and Hatfield, W. E. (1978) *Inorg. Chim. Acta31*, 1−4.
**52** Little, I. R., Straughan, B. P., and Thornton, P. (1986) *J. Chem. Soc.,Dalton Trans.*, 2211−2214.
**53** Khangulov, S. V., Sossong, T. M. J., Ash, D. E., and Dismukes, G. C. (1998) *Biochemistry37*, 8539−8550.
**54** Christianson, D. W., and Alexander, R. S. (1989) *J. Am. Chem. Soc.111*, 6412−6419.
**55** D'souza, V. M., Bennett, B., and Holz, R. C. (2000) *Biochemistry39*, 3817−3826.
**56** Concha, N. O., Rasmussen, B. A., Bush, K., and Hertzberg, O. (1996) *Structure4*, 823−836.
**57** Bounaga, S., Laws, A. P., Galleni, M., and Page, M. I. (1998) *Biochem. J.331*, 703−711.
**58** Fabiane, S. M., Sohi, M. K., Wan, T., Payne, D. J., Bateson, J. H., Mitchell, T., and Sutton, B. J. (1998) *Biochemistry37*, 12404−12411.
**59** Christianson, D. W., and Lipscomb, W. N. (1989) *Acc. Chem. Res.22*, 62−69.

**1** Abbreviations: Hepes, 4-(2-hydroxyethyl)-1-piperazineethanesulfonic acid; Tricine, *N*-tris(hydroxymethyl)methylglycine; LPA, l-leucinephosphonic acid; BuBA, 1-butaneboronic acid; AAP, aminopeptidase from *A. proteolytica*; blLAP, bovine lens leucine aminopeptidase; MetAP, methionine aminopeptidase; EPR, electron paramagnetic resonance.